Assessment of geometrical variability in 3D printed ZrO$_2$: Effects of printing and thermal post-processing

Erik Kornfellner [a,*], Filip Jelínek [b], Laszlo Jaksa [b], Anna Lebhard [c,d], Daniel Bomze [c], Martin Schwentenwein [c], Francesco Moscato [a,e,f]

[a] *Center for Medical Physics and Biomedical Engineering, Medical University of Vienna, Vienna, Austria*
[b] *ACMIT Gmbh, Wiener Neustadt, Austria*
[c] *Lithoz GmbH, Vienna, Austria*
[d] *TU Wien, Getreidemarkt 9/164-CT, Vienna, Austria*
[e] *Ludwig Boltzmann Institute for Cardiovascular Research, Vienna, Austria*
[f] *Austrian Cluster for Tissue Regeneration, Vienna, Austria*

ARTICLE INFO

ABSTRACT

3D printing is developing rapidly and enables the production of parts manufactured using different materials. These includes zirconium dioxide (ZrO$_2$), which can be of particular interest for bone tissue engineering and implantology. However, highly accurate part-dimensions are a must for these applications, which is why this study addresses geometrical deviations which occur during the printing process and thermal post-processing.

Six sets of test geometries with 50 individual features were 3D printed with two different ZrO$_2$ slurries (3 mol % yttria-stabilized ZrO$_2$) and scanned with a profilometer. After debinding and sintering, the profilometer scan was repeated and the deviations and shrinkage factors were determined.

A notable difference is observed when the same ceramic is processed using two different slurries. For instance, one used ceramic slurry, *LithaCon 210*, exhibits shrinkage factors of $shr_{XY} = 21.2 \pm 3.4\%$ ($n = 78$) and $shr_Z = 23.6 \pm 0.54\%$ ($n = 24$) for protruding structures, while the other ceramic slurry, *LithaCon 280*, shows shrinkage factors of $shr_{XY} = 21.7 \pm 3.3\%$ ($n = 78$) and $shr_Z = 24.5 \pm 0.55\%$ ($n = 24$).

Geometric deviations differed for intruding (like holes and slots) and protruding (like pillars) geometries, being more pronounced in case of intruding geometries, especially where printing overhangs occur.

Although the shrinkage during sintering needs further investigation, these experimental findings are a good starting point to validate and refine simulation models for shrinkage and improve production processes of 3D printed ceramics.

1. Introduction

From the Stone Age to the present day, human beings have always been in search of new materials to manufacture their tools and devices. Meanwhile, today's society can access an enormous range of different materials and manufacturing techniques. One of the recently introduced manufacturing methods is ceramic 3D printing [1]. Despite its relative infancy, there are already many interesting application areas, such as bone tissue engineering and implantology [2–4] or aerospace [5,6], where such high-performance materials with complex geometry are required.

Ceramic materials have already been developed for the most popular 3D printing processes. Ceramics can be produced by photo-curing stereolithography, selective laser sintering, direct ink writing, or binder jetting, among others [7–9]. The resulting prints differ by the porosity achieved, but also by geometrical variability due to the printing process, depending on the chosen type of fabrication and printer settings. Nonetheless, it is currently possible to additively manufacture ceramics with properties comparable to those fabricated by cold isostatic pressing [10].

It is of course essential to obtain an accurately fitting part after thermal post-processing, which all of these 3D printing processes require, namely debinding and sintering. For this purpose, the green parts, the freshly printed geometries that have not yet been sintered, are

printed in larger dimensions than the final geometry, as the parts shrink during sintering. To predict and fine tune the extent of shrinkage there are already some techniques available, such as adjusting the exposure in stereolithography, especially on the geometries borders [11,12]. It should also be considered that different slurry mixtures may behave differently during the fabrication process in lithography-based ceramic manufacturing (LCM), which belongs to the family of vat photopolymerization (VPP) processes. Theories and simulation models, in addition, are being established for determination of the shrinkage during sintering [13–16], primarily to avoid tedious trial and error, which is often a long and expensive way of part optimization. However, shrinkage of the 3D printed ceramic zirconium dioxide (ZrO_2) is still little investigated in a systematic way.

In order to develop such simulations for the auspicious material ZrO_2 experiments were conducted and measurement shrinkage data were collected. This study addresses complex printing geometries with different feature sizes and types of parts, which were printed with two different ZrO_2 slurries.

2. Methods

Three different 3D printable designs were fabricated with LCM to determine the change in printed feature sizes during the thermal post-processing. To fabricate ZrO_2, two different slurries, *LithaCon 210* and *LithaCon 280* (Lithoz GmbH, Vienna, Austria), both with 3mol% Y_2O_3, were used. Both slurries lead to ZrO_2 ceramics, but the binder composition varies. *LithaCon 280* has a higher crosslink density, therefore it creates stiffer green parts than *LithaCon 210* with the same amount of curing light exposure. Six samples per design and material have been fabricated with the ceramic 3D printer *CeraFab 7500* (Lithoz GmbH, Vienna, Austria), which is based on the principle of digital light processing (DLP), and cleaned with the cleaning solution *LithaSol 80* in a *CeraCleaning Station Ultra* (Lithoz GmbH, Vienna, Austria). This cleaning station operates similarly to an airbrush, where solvent is applied to the samples to remove excess slurry adhering to the samples.

The obtained green parts have been scanned with an optical profilometer (*Keyence VR-5000*, Keyence International, Mechelen, Belgium), before they were thermally post-processed for debinding and sintering. A second series of profilometer scans was then performed with the finished ceramic samples. With the used settings, this device achieves a resolution of 1 μm.

The flow chart in Fig. 1 shows the relation of the green parts and the finished parts to the other design steps, and what useful comparisons can be made from them.

2.1. Geometric features

The three different geometries, labeled A, B, and C, each had different geometric features. A 3D rendering of the geometries is shown in Fig. 2 and the features are listed below.

Geometry A consists of protruding structures in the form of both round and rectangular pillars. In contrast, Geometry B was designed to incorporate negative features, as slots and holes, which exhibit a range of sizes. This design choice allows for the investigation of how the printing process handles such variations in negative geometries. Lastly, Geometry C is characterized by overhanging bridges and angles, presenting unique challenges during the printing process. This geometry offers valuable insights into the printer's capabilities to produce complex structures with unsupported segments, providing information for optimizing print settings and support structures.

- Geometry A
  - 5 round pillars with 4 mm height and diameters of ⌀ 250 μm, ⌀ 500 μm, ⌀ 1 mm, ⌀ 2 mm and ⌀ 4 mm
  - 5 rectangular pillars with 4 mm height and side lengths of 250 μm, 500 μm, 1 mm, 2 mm and 4 mm
  - outer dimensions of 10 mm×13 mm
- Geometry B
  - 4 slots with a width of 250 μm, 500 μm, 800 μm and 1 mm
  - 7 rectangular holes with an edge length of 300 μm, 400 μm, 500 μm, 600 μm, 800 μm, 1 mm and 1.5 mm
  - 7 round holes with diameters from ⌀ 300 μm, ⌀ 400 μm, ⌀ 500 μm, ⌀ 600 μm, ⌀ 800 μm, ⌀ 1 mm and ⌀ 1.5 mm
  - a fillet edge with a variable radius from 0 to 2.5 mm
  - an outer dimension of 11 mm
- Geometry C
  - 9 overhanging bridges with 1 mm gap underneath and lengths of 500 μm, 700 μm, 1 mm, 1.2 mm, 1.5 mm, 1.8 mm, 2 mm, 2.5 mm and 3 mm
  - an overhanging quarter circle with a radius of 2 mm
  - 5 overhangs with angles of 15°, 30°, 45°, 60° and 75°

2.2. Printer settings

The samples have been printed in two batches, nine samples each, and the models have been sliced with *CeraFab-DP* (Lithoz GmbH, Vienna, Austria). The build time was approximately 10.5 hours per batch. The used parameters are listed in Table 2. Also an overexposure correction was used, reducing the illuminated area by one pixel per side.

The expected shrinkage *shr* is given by the supplier (Lithoz) of the used ceramic slurries, which also determines the necessary compensation factors *cf*, are listed in Table 1. For *LithaCon 210* they amount to $shr_{XY,exp} = 21.3\%$ in XY direction and $shr_{Z,exp} = 22.8\%$ in Z direction, and for *LithaCon 280* to $shr_{XY,exp} = 21.5\%$ and $shr_{Z,exp} = 23.5\%$. The relationship between compensation factor *cf* and shrinkage *shr* is shown in Equation (1) and leads to the shrinkage compensation factors $cf_{XY} = 1.271$ and $cf_Z = 1.295$, which were used to upscale the digital model before printing, to achieve the desired sizes after the thermal post-
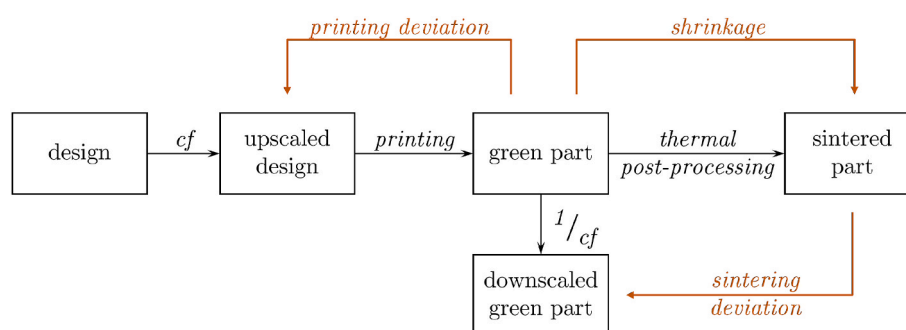

Fig. 1. Process flowchart showing the path from the design to the finished ceramic part. The most important evaluations are the comparison of the printed green part with the upscaled design (with the correction factor *cf*), as well as the comparison of the finished sintered part with a digitally downscaled model of the green part, to evaluate changes during the thermal post-processing.
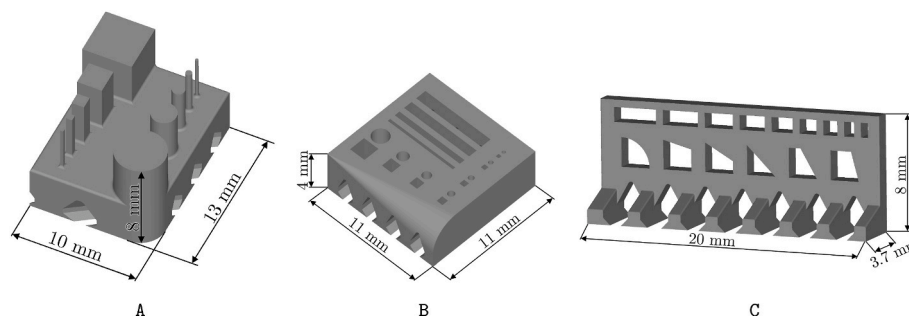
Fig. 2. 3D renderings of the three different test geometries.

Table 1
Shrinkage compensation factors used for the two different slurries.

direction	LithaCon 210	LithaCon 280
XY (cf_{XY})	1.271	1.274
Z (cf_Z)	1.295	1.307

Table 2
Printer settings and technical properties.

parameter	value
layer thickness (as printed)	25 μm
exposure time	1.5 s
exposure intensity	100 mW/cm^2
exposure energy	150 mJ/cm^2
lateral resolution (pixel pitch)	57 μm

processing.

$$shr = \frac{cf - 1}{cf} \tag{1}$$

2.3. Thermal post-processing

After printing and cleaning the parts were stored at 40 °C before undergoing further debinding and sintering. The debinding and sintering took 94 h and was performed in the *Nabertherm HTCT 08/16* sintering oven (Nabertherm GmbH, Lilienthal, Germany) with a maximum temperature of 1450 °C. The time course for the thermal post-processing was set as recommended by Lithoz, and is shown in Fig. 3.
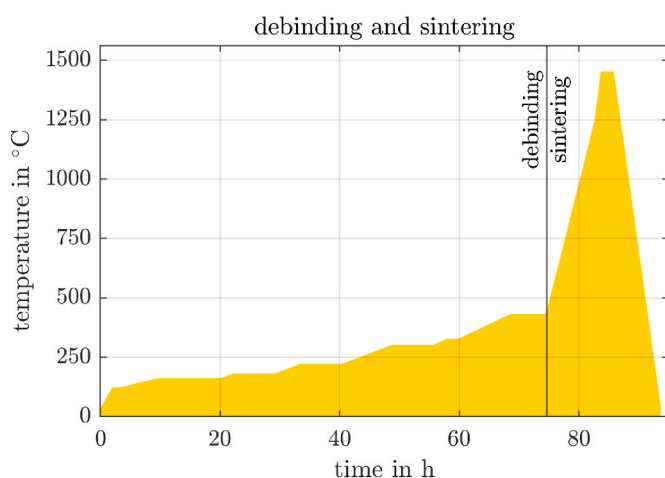

Fig. 3. These diagram shows the temperature during debinding and sintering. The maximum temperature reached during sintering is 1450 °C.

2.4. Profilometer measurements

The same measurements were performed on the profilometer data of the green parts and the post-processed parts, using the software *VR Series Analyzer* (Keyence International, Mechelen, Belgium). The width, length and diameter of pillars and holes have been measured at half height. The radii were measured by adding a best fit circle to the profile section. The height of pillars were measured by comparing the average height of the pillars top surface to the average height of the specimens base surface. To measure the angles on the specimen, straight lines have been fitted along the profile edges, excluding rounded corners. Angles were measured between these lines.

3. Results

All 36 samples have been printed successfully. A finished part for each of the three different test geometries is shown in Fig. 4.

Cleaning the parts is quite a complex process, during which they are first carefully detached from the printer's building platform using a razor blade and then sprayed with the cleaning solution, which is left on for a few minutes to dissolve any uncured slurry and then blown away with an airbrush from a safe distance until the green bodies are dry. If there are any remaining layers of uncured material, they would flake off during sintering. These residues on the sintered part can be scraped off, for example with an ultrasonic scaler. Care was taken, that the sintered parts were free of surface soiling and flaking residues.

3.1. Protrusions

Protruding geometries, such as the pillars of test geometry A and the outer dimensions of the test parts A and B, underwent a lateral shrinkage of $shr_{XY} = 21.2 \pm 3.4\%$ ($n = 78$) for *LithaCon 210* and $shr_{XY} = 21.7 \pm 3.3\%$ ($n = 78$) for *LithaCon 280*. In Z direction, the shrinkage of the pillars of test geometry A was $shr_Z = 23.6 \pm 0.54\%$ ($n = 24$, *LithaCon 210*) and $shr_Z = 24.5 \pm 0.55\%$ ($n = 24$, *LithaCon 280*).

The total error from the finished part to the design is made up of the printing error and the thermal treatment error. The deviations of pillars and outer dimensions are shown in Fig. 5. It is shown, that most pillars deviate from the design about ± 50μm in XY direction. The pillar height is below the design for all specimen. While the printing deviations were comparably small, large deviations occurred in the shrinking process during thermal post-processing. Especially the outer dimensions have very low relative total errors ($< 1\%$), although the absolute total error is around 100 μm. Only round pillars with diameter $d = ⌀250$ μm and $d = ⌀500$ μm feature a lesser shrinkage ratio, but higher standard deviation of those, than most other pillars ($shr = 16\%$ to 19%).

Regarding the outer dimensions, it has been observed that the parts shrink more than expected. This resulting in noticeably smaller dimensions than designed. In addition, the *LithaCon 280* samples are also printed to small, compared to the *LithaCon 210* samples. All exact values are shown in the supplement – Table 3.
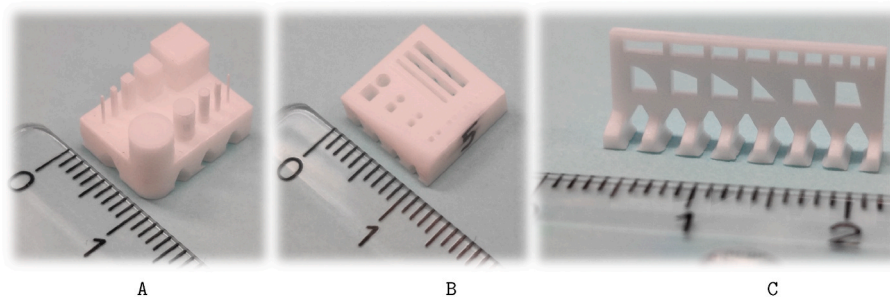
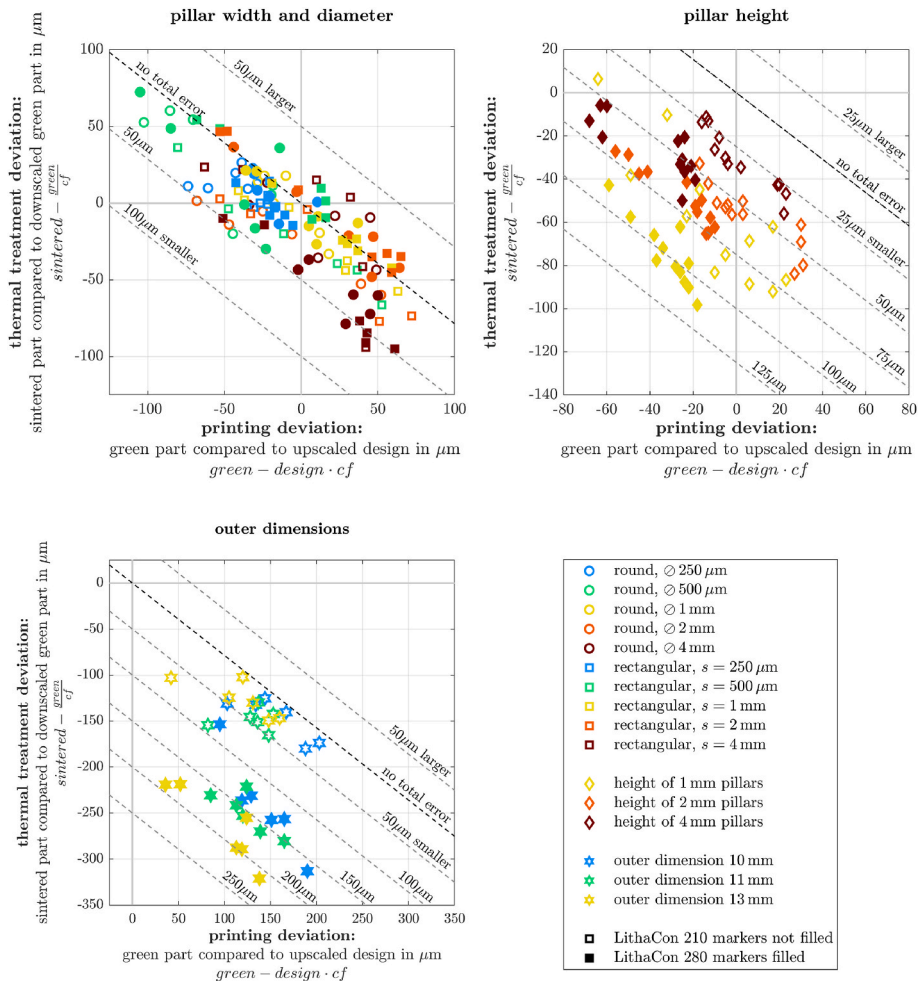**Fig. 4.** The three different test geometries in sintered state. The unit of the scale is centimeters.

Fig. 5. Scatter plot showing the deviations occurred during printing (X axis) and thermal postprocessing (Y axis) in the individual positive structures. Upper left: width and diameter of pillars, showing features transversal to the printing direction. Upper right: height of the pillars, showing features in printing direction. Lower left: showing outer dimensions, transversal to the printing direction. The diagonal lines indicate the difference from the finished part to the digital design and correspond to the shrinking factor of *LithaCon 210*.

3.2. Holes and slots

Inward features behave similarly to the outward ones just discussed. For both materials, larger structures, here holes above s = 800 μm, exhibit shrinkage in the range of approximately 19%–23%. In contrast, smaller structures show lower shrinkage factors, going down to 10%. Additionally, the dispersion of shrinkage values increases as the structures become smaller.

The deviation of the green parts holes and slots dimensions to the targeted design is ranging around 100μm smaller to 25 μm larger, as

shown in Fig. 6. However, there is a significant difference between the two different slurries. While all holes in the *LithaCon 280* samples are consistently clear, the 300 μm and 400 μm holes in the *LithaCon 210* samples, with one exception, are clogged. Similarly, the length of the narrowest slot in the *LithaCon 210* samples is significantly reduced, and its width is nonuniform. All exact values are shown in the supplement – Table 4.
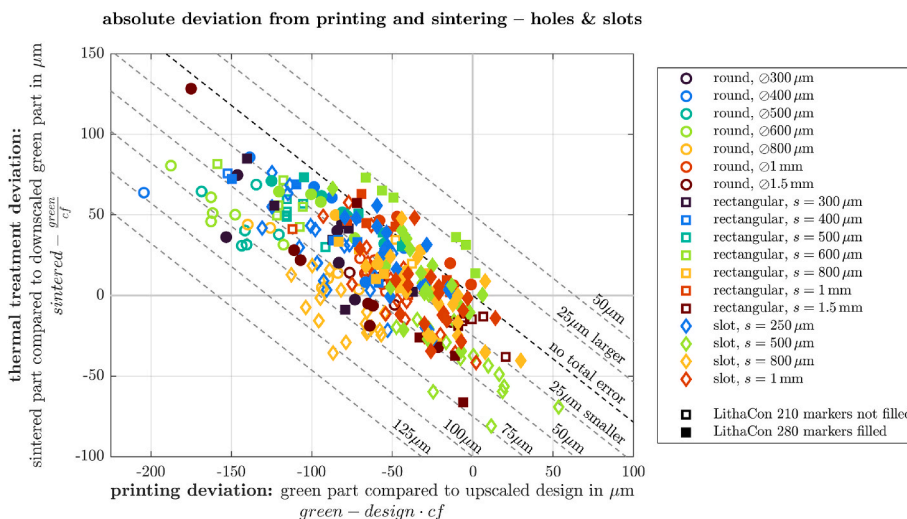
Fig. 6. Scatter plot showing the deviations occurred during printing (X axis) and thermal post-processing (Y axis) in the individual negative structures. The diagonal lines indicate the difference from the finished part to the digital design and correspond to the shrinking factor of *LithaCon 210*.

3.3. Radii

Two different types of radii were tested, on specimen geometry C was a quarter circle with an overhanging radius $r = 2$ mm, while specimen geometry B had a fillet radius with changing radius, where the radius has been measured at 4 different positions. The average shrinkage of the radii was 19.8%. However the overhanging radius has shrunk less than the others, but features a higher standard deviation $shr = 17.1 \pm 9.23\%$. The deviations occurring from printing and thermal post-processing are shown in Fig. 7, the exact values are shown in the supplement – Table 6.

3.4. Overhanging bridges

Printing and sintering worked for all nine bridges with a length from 500 μm of up to 3 mm. The lengths of the printed bridges vary slightly. Most measurements on *LithaCon 210* samples range from 0 to 50 μm larger than the design, while *LithaCon 280* samples tend to be smaller than the design, in a range of 0 to −100 μm, as shown in Fig. 9. Although the bridges for both slurries were printed slightly wider than designed, likely due to overexposure correction, the differences arise from the significantly greater shrinkage of *LithaCon 280* samples.

Depending on the length, various effects were observed which cause the underside of the bridge to deviate from the ideal flat shape. Very narrow bridges are printed correctly and are almost flat on the upper side. For the slightly larger bridges, deflections can be seen. This is most likely due to overpolymerization in the corners and from stress on the thin printed layer from gravitation or pull of from the light window. As a reminder, the parts are printed hanging upside down. This results in the bridge being higher in the middle than on the sides, as with a vault, as shown in Fig. 8a. In the longest bridges tested (3 mm), a compression can be seen, see Fig. 8b. Presumably, the sagging bridge is compressed in the opposite direction when re-entering the slurry bath. As a result, these bridges are less high in the middle than on the sides. These effects concerning the bridge geometry already occur in the green part. A notable difference between the two slurries is also observed. While the deviations during the printing process remain relatively constant for *LithaCon 280*, they steadily increase with shorter bridges for *LithaCon 210*, as shown in Fig. 10. All exact values are shown in the supplement – Table 5.
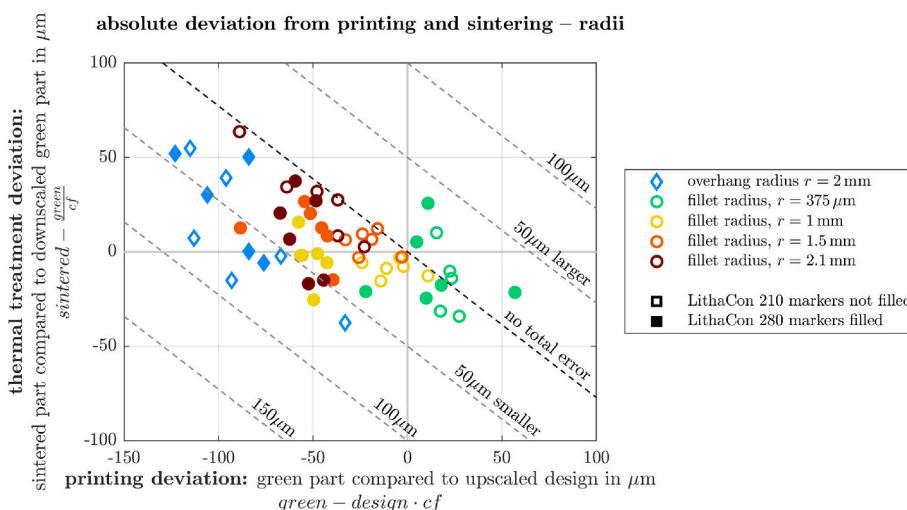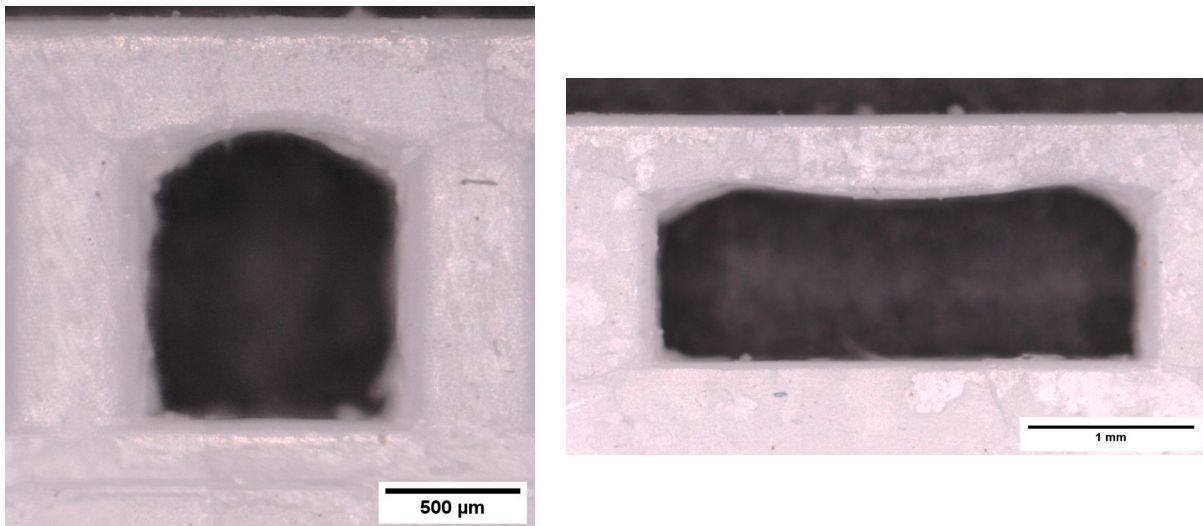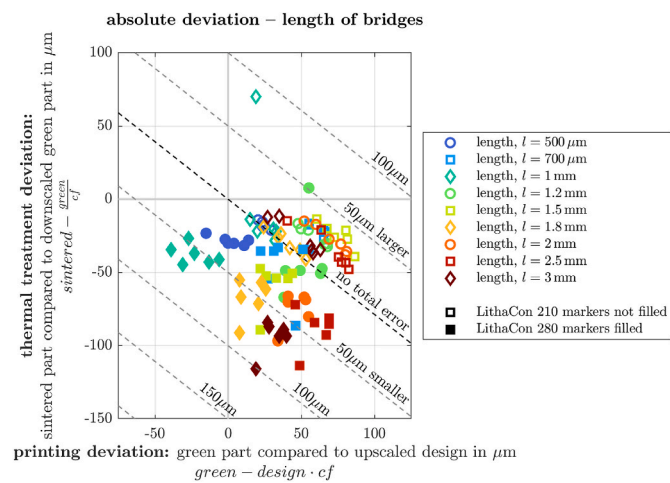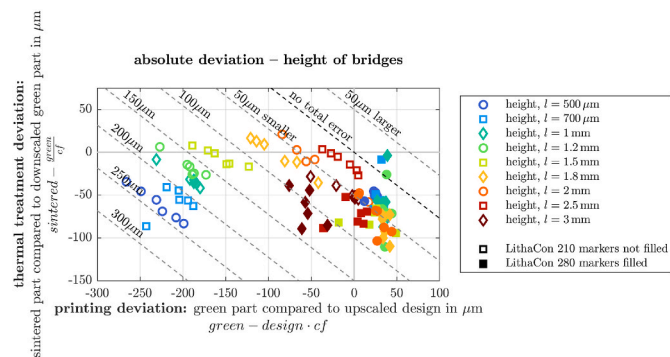

Fig. 7. Scatter plot showing the deviations occurred during printing (X axis) and thermal post-processing (Y axis) on the individual radii. The diagonal lines indicate the difference from the finished part to the digital design and correspond to the shrinking factor of *LithaCon 210*.

Fig. 8. Microscope image from the profilometer, white sample on dark background. The printing direction of the 3D printer is from bottom to top in the picture, as the parts are made hanging upside down. The bottom side of the recess, which is printed first, is flat in both cases. **(a)** Overhang with a length of l = 1 mm. The upper side, where the printer has to bridge over the recess, is arched outward. Most likely due to overpolymerization effects in the corners and Z compensation. **(b)** Overhang with a length of l = 3 mm. The top side, which is printed as a overhanging bridge, is curved. The top of the sample is flat again.


Fig. 9. Scatter plot showing the deviations occurred during printing and thermal post-processing on the bridge structures with different lengths. The diagonal lines indicate the difference from the finished part to the digital design and correspond to the shrinking factor of *LithaCon 210*.

Fig. 10. Scatter plot showing the deviations occurred during printing and thermal post-processing on the bridge structures. All bridges have a designed height of 1mm. The diagonal lines indicate the difference from the finished part to the digital design and correspond to the shrinking factor of *LithaCon 210*.

3.5. Overhanging angles

The deviation of the sintered parts angles to the designed angles are smaller than those of the green parts angles. This is an indication that the parts shrink differently in the XY direction than in the Z direction, as expected when selecting the corresponding correction factors. In all these cases, a higher shrinkage in Z direction also means that the angles become more acute. The difference of the measured angles to the designed values in the finished state are shown in Fig. 11. With the used correction factors for *LithaCon 210*, the upscaled designs for the green-parts have the following angles: $15.27°$, $30.47°$, $45.54°$, $60.46°$, $75.27°$ and for *LithaCon 280*: $15.37°$, $30.64°$, $45.73°$, $60.63°$, $75.36°$. The exact
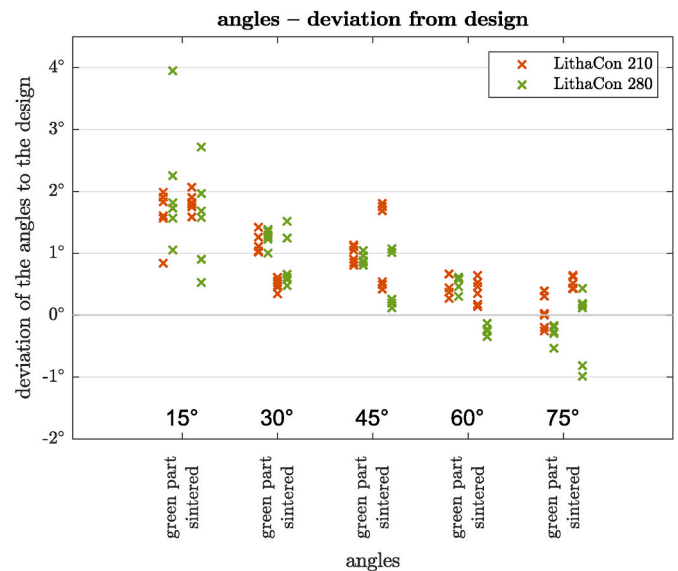
Fig. 11. Plot of the measured angles. All median values are shrinking during the sintering process. For each angle, the green part is shown on the left side, while the markers on the right side show the measurement values of the sintered part for comparison. The number of measurements for all angles is $n = 5$. (For interpretation of the references to colour in this figure legend, the reader is referred to the Web version of this article.)

values are shown in the supplement – Table 7.

4. Discussion

The experimental findings presented in this study reveal valuable insights into the dimensional variations observed in 3D printed green parts and their subsequent sintered analogues. The key observations revolve around the origin of geometrical deviations, which were split to variations from printing and thermal post-processing.

It is noticeable that the expected and measured shrinkage factors fit better for structures in XY directions than in Z direction, which aligns with the printing direction. However, concerning the outer dimensions, it was demonstrated that the samples shrink significantly more than expected. The samples precisely segregate into the two groups based on the slurry used in their production, as illustrated in Fig. 5.

The total deviation of pillars and holes, both measured in the XY direction, is nearly equal. This is primarily due to the employed overexposure correction. Overexposure means, that the excessive energy applied during printing leads to unintended curing of the slurry beyond the desired geometry, giving rise to the observed deviations. These data demonstrate that well-tuned overexposure correction, in this case 57 μm, can yield good results. Without this correction, positive structures would consistently become too large, and negative structures would become consistently too small or even clogged. The offset caused by overexposure is nearly constant and could thus be corrected using the applied overexposure correction.

One observation that can be made from the clogged holes is that the surfaces of the green parts may not have been perfectly clean of slurry prior to sintering, or that small holes may have closed due to overexposure.

Regarding the heights of the overhanging bridges, the *Lithacon 210* samples show considerable deflections that increase with the length of the bridge. This is probably due to the thin bridges sagging during the printing process. The lower deflection observed in *Lithacon 280* could be attributed to the higher crosslink density of the binder, resulting in stiffer green parts compared to *Lithacon 210*.

As for shrinkage during debinding and sintering, the measured values show a certain scatter, but the shrinkage factors for protruding and inward structures are in a similar range. A different shrinkage depending on the direction, XY or Z, was already expected and can be clearly observed. A good example of this is the printed angles where one axis was printed in layer and the other axis was printed across the layer. Since different correction factors were used for this, the median values adapt better to the nominal values after sintering. Naturally, a better correlation between the green parts and the sintered parts mean a more uniform shrinkage of this geometry feature.

To enable mass production with this technology, the authors recommend designing all parts with printability in mind, but specifying the sizes that the finished part should have. The adjustment of the geometries to be printed, taking into account the geometric changes that occur during manufacturing, should be done during slicing. This approach also allows to create print files for different 3D printers.

One reason for the scattering of the measured shrinkage can of course be an inaccuracy in the measurement with the profilometer, especially due to the glossy high reflective surface. One reason for inconsistently thick features could be uneven exposure of the DLP light source. At some positions the exposure is higher and the parts at these locations get therefore larger [17]. Also a reason for printing deviations could be the positioning on the building platform. Since the matrix display of the 3D printer has a specific pixel pitch, only discrete sizes can be produced. But of course it cannot be ruled out that parts of the same geometry shrink differently during debinding and sintering.

There are potential factors contributing to variations in the measured shrinkage during thermal post-processing. The positioning of parts in the kiln and the use of different furnaces are identified as critical elements that can influence shrinkage. Moreover, the specific ceramic material used and its associated sintering temperature prevent generalizability of shrinkage results for different ceramics or other thermal treatment parameters.

5. Conclusion

In this study, the geometric accuracy of 3D-printed ZrO_2 was investigated and experimental data was collected to enable to form a basis for further improvement of print files for more accurate print jobs. Three different test specimens were each 3D printed six times from two different slurries each, scanned with a profilometer, sintered and rescanned. Deviations of the printed green parts from the digital design could be identified, and shrinkage during the printing process was investigated. The geometries tested included columns, holes, slots, overhangs, radii and overhangs, covering all printable geometries in their simplest form. Overexposure correction was utilized to prevent a size mismatch between protruding geometries, like pillars and outside dimensions, and negative geometries, like holes and slots.

This study sheds light on the complex interplay between overexposure effects, shrinkage, and dimensional variations in 3D printed ceramic parts. By exploring the proposed solutions, future research can pave the way for enhanced print results and more precise control over dimensional accuracy. Moreover, a deeper investigation of the factors influencing shrinkage, including positioning in sintering ovens and material variations, would be instrumental in refining the understanding of these intricate processes.

CRediT authorship contribution statement

Erik Kornfellner: Conceptualization, Investigation, Methodology, Project administration, Visualization, Writing – original draft. **Filip Jelínek:** Resources. **Laszlo Jaksa:** Resources. **Anna Lebhard:** Resources. **Daniel Bomze:** Resources. **Martin Schwentenwein:** Resources. **Francesco Moscato:** Funding acquisition, Supervision, Writing – review & editing.

Declaration of competing interest

The authors declare that they have no known competing financial interests or personal relationships that could have appeared to influence the work reported in this paper.

Appendix A. Supplementary data

References

[1] Zhangwei Chen, et al., 3D printing of ceramics: a review, J. Eur. Ceram. Soc. 39 (4) (2019) 661–687, issn: 0955-2219.

[2] Taha Khalaf Ahmad, et al., Bone tissue engineering through 3D bioprinting of bioceramic scaffolds: a review and update, English: Life 12.6 (2022). Cited by: 2; All Open Access, Gold Open Access, Green Open Access. issn: 20751729.

[3] D.J. Cohen, et al., Novel osteogenic Ti-6Al-4V device for restoration of dental function in patients with large bone deficiencies: design, development and implementation, Sci. Rep. 6 (1) (Feb. 8, 2016) 20493 issn: 2045-2322.

[4] Franz E. Weber, Reconsidering osteoconduction in the era of additive manufacturing, Tissue Eng. B Rev. 25.5 (Apr. 18, 2019). Publisher: Mary Ann Liebert, Inc., publishers, pp. 375–386. issn: 1937-3368.

[5] Gautier Mazingue, et al., 3D printed ceramic antennas for space applications, in: 2020 14th European Conference on Antennas and Propagation, EuCAP, 2020, pp. 1–5.

[6] Tarunpreet Singh, Sanjeev Kumar, Sehgal Shankar, 3D printing of engineering materials: a state of the art review, International Conference on Aspects of Materials Science and Engineering 28 (Jan. 1, 2020) 1927–1931, issn: 2214-7853.

[7] Lim Chin Hwa, et al., Recent advances in 3D printing of porous ceramics: a review, Curr. Opin. Solid State Mater. Sci. 21 (6) (2017) 323–347, issn: 1359-0286.

[8] Jia-Chang Wang, Hitesh Dommati, Sheng-Jen Hsieh, Review of additive manufacturing methods for high-performance ceramic materials, Int. J. Adv. Des. Manuf. Technol. 103 (5) (Aug. 1, 2019) 2627–2647, issn: 1433-3015.

[9] Pragnya Kunchala, Keerti Kappagantula, 3D printing high density ceramics using binder jetting with nanoparticle densifiers, Mater. Des. 155 (2018) 443–450, issn: 0264-1275.

[10] David Carloni, Guangran Zhang, Yiquan Wu, Transparent alumina ceramics fabricated by 3D printing and vacuum sintering, J. Eur. Ceram. Soc. 41 (1) (2021) 781–791, issn: 0955-2219.

[11] Cheng Zhang, et al., Dimensional retention of photocured ceramic units during 3D printing and sintering processes, Ceram. Int. 47 (8) (2021) 11097–11108, issn: 0272-8842.

[12] Ege Guven, Yigit Karpat, Melih Cakmakci, Improving the dimensional accuracy of micro parts 3D printed with projection-based continuous vat photopolymerization using a model-based grayscale optimization method, Addit. Manuf. 57 (2022) 102954 issn: 2214-8604.

[13] Alexander Safonov, et al., Numerical simulation of sintering for 3D-printed ceramics via SOVS model, Ceram. Int. 45.15 (2019) 19027–19035, issn: 0272-8842.

[14] Eugene A. Olevsky, Theory of sintering: from discrete to continuum, Mater. Sci. Eng. R Rep. 23 (2) (June 30, 1998) 41–100, issn: 0927-796X.

[15] Torsten Kraft, Hermann Riedel, Numerical simulation of solid state sintering; model and application, 8th International Conference on Ceramic Processing 24.2 (Jan. 1, 2004) 345–361, issn: 0955-2219.

[16] Suk-Joong Kang, Sintering: Densification, Grain Growth & Microstructure, Jan. 2005.

[17] Erik Kornfellner, et al., Elastic and dimensional properties of newly combined 3D-printed multimaterials fabricated by DLP stereolithography, Frontiers in Materials 10 (2023) issn: 2296-8016.